

Printed nanoparticulate composites for silicon thick-film electronics*

D. T. Britton[‡] and M. Härting

Department of Physics, University of Cape Town, Rondebosch 7701, South Africa

Abstract: The production of active semiconductor thick-film components typically involves the deposition of precursor materials and subsequent thermal processing to produce a massive semiconductor layer. In this paper, we present electronic materials, based on nanoparticulate silicon, to produce the active semiconducting layer, which can simply be printed onto low-temperature substrates such as paper. Particular emphasis will be given to the structure, morphology, and composition of the nanoparticles, which are produced by either gas-phase decomposition of silane or mechanical attrition of bulk silicon. Of further importance are the electrical characteristics of the composite materials, in which the active semiconductor is formed from an interconnecting backbone of silicon particles. These will be discussed for example structures, including junction field effect transistors (FETs), insulated-gate FETs, and photodiodes.

Keywords: composites; nanoparticulates; thick-film electronics; nanoparticulate silicon; junction FETs; insulated-gate FETs; photodiodes.

INTRODUCTION

For over half a century, thick-film printing has been applied as an efficient and cost-effective alternative to other methods of patterning passive electronic components and circuitry [1]. Conventional thick-film inks consist of a colloidal, usually microcrystalline, suspension of a metal or dielectric material in a vitreous or polymeric binder, which on curing forms a continuous interconnected layer of the base material. Depending on the material and application, the curing stage may involve one or more different processes, ranging from simple air drying under ambient conditions to high-temperature sintering. The former is, obviously, the goal for inexpensive mass production of a wide variety of flexible low-temperature substrates such as polymer films, paper, and textiles.

The production of active semiconductor thick-film components typically involves the deposition of precursor materials and subsequent thermal processing to produce a massive semiconductor layer. A good example of an established technology is the use of CdSe and CdS in solar panels [2]. Similarly, massive sintered silicon is gaining application as an alternative to silicon wafers in a variety of applications [3]. There is, however, to date no commercial inorganic semiconductor equivalent of low-temperature thick-film materials for passive components.

In this paper, we present the inclusion of nanoparticulate silicon as the active layer in electronic materials, which can be printed using simple techniques on low-temperature substrates such as paper. Particular emphasis will be given to the structure, morphology, and composition of the nanoparticles,

*Paper based on a presentation at the 3rd IUPAC Workshop on Advanced Materials (WAM III), Stellenbosch, South Africa, 5–9 September 2005. Other presentations are published in this issue, pp. 1619–1801.

[‡]Corresponding author

which are produced by either gas-phase decomposition of silane or mechanical attrition of bulk silicon. Of further importance are the electrical characteristics of the composite materials, in which the active semiconductor is formed from an interconnecting backbone of silicon particles. These will be discussed for example structures, including metal-insulator-semiconductor field effect transistors (FETs) and photodiodes.

NANOPHASE SILICON

Nanophase silicon is currently a material of significant research and applied interest, from two convergent directions. As a thin-film electronic material, nanocrystalline silicon is seen as a replacement for hydrogenated amorphous silicon (a-Si:H), because of its higher stability against in-service degradation and better electrical properties, such as carrier mobility, approaching that of bulk polycrystalline silicon. Nanocrystalline layers can be grown using the same chemical vapor deposition (CVD) techniques as for a-Si:H [4–6], at high growth rates, and can also be electrically doped [5].

On the other hand, single silicon nanoparticles are becoming a widely studied system at both a fundamental level for single electron states (quantum dots) and applications, such as light-emitting diodes (LEDs) and photonic arrays, based on their associated optical transitions [7,8]. For these applications, the nanoparticles need to be dispersed in a dissimilar matrix which is optically transparent at the required frequency. In most cases, this is silica, with the particles being produced by various segregation mechanisms from nonstoichiometric silicon oxides [7,8]. Low concentrations of small silicon nanocrystals can also be produced by annealing after ion implantation of silica with silicon [9]. Disperse silicon nanocrystals can also be grown in an a-Si:H matrix by postdeposition annealing [10] or layer-by-layer growth [11]. Isolated quantum dot structures can also be prepared by embedding free nanoparticles in a polymeric matrix [12], which would allow low-temperature processing and layer deposition on a variety of large-area substrates. More often, however, the optical properties of free nanoparticles are studied with the particles in a colloidal suspension.

Free nanoparticles can be produced by either a bottom-up chemical synthesis, or a top-down size reduction of bulk material. In the case of silicon, this has traditionally meant one of two forms of thermal processing: pyrolysis of silanes [13–16]; or evaporation of bulk silicon in an inert atmosphere [17,18]. The method most widely used is decomposition of silane gas, which can be achieved using simple thermal pyrolysis [13,14] or laser decomposition [15], to produce particles with size distributions below 100 nm. Smaller particles, around 10 nm diameter or less, can be produced through cluster generation in processes similar to hot-wire CVD [16] or plasma-enhanced CVD [14], or by thermal reduction of silicon-containing organic compounds, such as diphenylsilane, in supercritical fluids at high pressure [19]. Soft chemical synthesis methods for silicon nanoparticles are limited by their complexity, involving multistage synthesis [20], or growth in inverse micelle structures [21], as well as by their low yield. Besides thermal methods, the main top-down approach to the production of micro- and nanoparticles from bulk material is mechanical attrition, using a variety of mill types. The method most commonly applied to silicon is ball milling [22,23], by which particles in the 100-nm size range can be produced. Reactive ball milling using aluminum to reduce silica, both of which grind more easily than silicon, has also been reported [24].

In many respects, the development of thick-film silicon technology has much in common with the study and application of compact nanocrystalline silicon produced by CVD, in that the primary focus is on the bulk semiconducting properties, and the production of electronic devices. Both are potential replacements for a-Si:H and are appropriate for inexpensive large-area devices fabricated on flexible substrates such as paper [25]. However, in the case of printed electronics, the compact layer is produced from an interconnected network of essentially free silicon nanoparticles, held together by a polymeric binder. Unlike the disperse composites being investigated for the optical properties of their localized states, there should be a direct semiconducting path through the material, with the semiconducting behavior provided by the particles themselves and not the matrix.

SAMPLE PREPARATION AND CHARACTERIZATION

Nanoparticulate silicon

Nanoparticulate silicon was produced by mechanical milling of bulk silicon from three different sources. For N- and P-type material, single-crystalline material in the form of 4-inch Czochralski-grown silicon wafers was used as the original feedstock. The N-type material was a (100) oriented, antimony-doped wafer of resistivity $3.0 \pm 0.1 \Omega\text{cm}$. The P-type material was boron-doped with a resistivity of $440 \pm 20 \Omega\text{cm}$.

A further source of bulk silicon was 2503 grade silicon metal, provided by Silicon Smelters (pty.) Ltd., Polokwane, South Africa. According to the manufacturer's analysis, the purity of this material is 99.4 %, with the main impurities being Fe at 0.21 % and Al at 0.144 %. Other specified impurities were Ca, Ti, Cr, P, and Ni with concentrations, in ppm, of 230, 129, 62, 43, and 18, respectively. As this material was provided in a granular form, it was not possible to determine its bulk electrical properties before preparation of the nanopowder. It is, however, like all metallurgical grade silicon, expected to be strongly N-type.

Nanophase powder was produced from the three bulk materials by milling in an 800 W Siebtechnik laboratory orbital pulverizer (Scheibenschwingmühle), equipped with a 52100 chrome steel pestle and mortar. 5 g of broken bulk silicon was milled in each run. After milling, the pestle was rinsed with ethanol to produce a suspension of the nanopowder. After centrifuging or allowing to settle naturally, the particles remaining in suspension were decanted.

For comparison, commercially obtained nanophase silicon powder, from MTI Corp., Richmond, California, was also studied. These particles were produced by laser pyrolysis of pure silane, and had a nominal maximum particle size of 50 nm, with the powder having a specific area greater than $80 \text{ m}^2 \text{ g}^{-1}$. Its purity was specified at >98 % on shipping, with the only detectable impurity being oxygen. This powder should, therefore, be nominally intrinsic and is referred to as such throughout this work, although light N-type doping could be expected due to the presence of oxygen.

For the powders, morphology was investigated using a LEO 912 transmission electron microscope (TEM) at 120 keV. To prepare the samples, the suspensions of particles in ethanol were simply dried at 60 °C onto standard carbon-coated copper TEM grids. A Leica Stereoscan S440i, operating in secondary electron mode, was used for the scanning electron microscopy (SEM) studies of the printed layers. At an operating beam energy of 20 keV, the estimated resolution of the images is 10 nm.

Electron diffraction patterns were also recorded during the TEM measurements. For N- and P-type material, the microstructure of the dry powder was additionally studied using X-ray diffraction. For these measurements, a Bruker AXS D8 Discover diffractometer, with Cu K α radiation was used. The diffraction pattern was measured over a 2θ range of 10 to 85° in steps of 0.02°.

The hydrogen and oxygen concentrations were determined in the nanopowders by ion beam analysis methods, using the 5.5 MeV single-ended van der Graaf accelerator at iThemba LABS, Faure, South Africa. The total hydrogen concentration was determined by elastic recoil detection analysis (ERDA) with 3 MeV helium ions as the projectile. The incident angle was 15°, and the forward-scattered protons were detected at a scattering angle of 30°. Oxygen was probed using the 3.05 MeV O(α,α)O resonance, at incidence and scattering angles of 10 and 165°, respectively. To obtain quantitative information, the energy distribution of the scattered particles was modeled using the RUMP package [26].

Silicon thick-film inks

Various formulations of inks based on nanoparticulate silicon, with different inert polymer binders and solvents, have been studied. In this work, we focus on two of the most promising practical binder materials: cellulose acetate butyrate (CAB), and acrylic screen printing base. The former is soluble in most organic solvents, including acetone and chloroform, and is the base of many commercial lacquers. The

latter is an autopolymerizing water-soluble monomer, used as a base for many paints, varnishes, and inks. Both materials are widely accepted to be nontoxic and environmentally neutral, if not friendly. Other binders tested include other soluble polymers such as polystyrene and auto-polymerizing polyesters.

Particle-to-binder volume ratios around 90 % are necessary to produce uniform semiconducting layers. For the soluble polymer binders (e.g., CAB and polystyrene), the solid polymer was dissolved in a solvent to produce a liquid base. In all cases, the nanoparticulate silicon was dispersed in the ink base, and the viscosity was adjusted by addition of a suitable thinner to the liquid base. For CAB, chloroform was used as both the original solvent and thinner, whereas for the liquid acrylic and polyester bases, both ethanol and commercial lacquer thinners proved equally suitable.

The printed layers were characterized in terms of their morphology using SEM. A Leica Stereoscan S440i, operating in secondary electron mode, was used at an operating beam energy of 20 keV. The estimated resolution of the images was 10 nm.

For electrical characterization using Hall effect measurements, the inks were hand-printed as approximately 100- μm -thick films on 80 g m^{-2} bond paper substrates using a glass roller. After drying, the coated paper substrates were cut to a size of 10 \times 5 mm. After mounting on a thick card base, electrical contacts were made using DuPont 5000 silver conductor. Hall effect measurements, with simultaneous determination of the resistance, were performed at room temperature using a 0.125 T permanent magnet. Because the carrier mobilities can be very variable in Czochralski silicon, the bulk mobilities and carrier concentrations were determined using the same Hall effect set-up as that used for the study of the nanoparticulate layers. The carrier mobilities of the bulk material were 2.3 $\text{cm}^2 \text{V}^{-1} \text{s}^{-1}$ and 0.45 $\text{cm}^2 \text{V}^{-1} \text{s}^{-1}$ for the N- and P-type wafers, respectively.

Doped silicon inks were produced by the addition of an ionic salt, either an alkali halide or rare earth halide. Examples of both NaCl and MgCl_2 are shown here. The quantity of binder was kept constant, at an amount equivalent to 8 % by volume of the undoped composition. Doped inks were also deposited directly onto TEM grids, for investigation by energy-dispersive X-ray fluorescence in scanning transmission electron microscopy (STEM) mode to determine the species responsible for doping.

Electronic devices

Figure 1 shows simple schematics of two example devices: a metal insulator FET (MIS-FET), with a bottom-gate geometry, and a NIP photodiode. For both devices, the substrate material was plain 80 g m^{-2} bond paper, which was used in its as-received condition. No particular precautions or prior treatment, beyond normal considerations of cleanliness and cross-contamination, were applied to the substrates or inks before printing.

Using a commercially available silver ink (DuPont 5000 conductor) a thin silver strip of 1-mm width was then printed, using a doctor blade, to serve as the gate contact. Other areas of the substrate were masked out with a stencil cut from adhesive tapes. The thickness of the silver layer after printing is about 10 μm . The gate layer was allowed to dry overnight under ambient conditions, after which a thin layer of the binder material, without silicon, was printed on it using the same approach. The insulating layer serves both the purpose of the gate insulator in the FET structure and also isolates the active layer from the substrate, to minimize shunt resistances.

Both CAB and the acrylic base form a thin flexible layer after curing in ambient air for about an hour, with the drying time for CAB being considerably faster. With the aid of a stencil and doctor blade, a thin coating of the semiconducting ink was then printed on the insulator layer to serve as the active layer for the transistor. Finally, the source and drain contacts were printed with a rubber stamp using the same silver conductor. The resulting source-drain separation, with this basic procedure, is typically between 0.3 and 0.5 mm. For a top-gate structure, the build sequence is reversed, with the source and drain contacts being printed with the doctor blade technique, and the gate contact stamp printed.

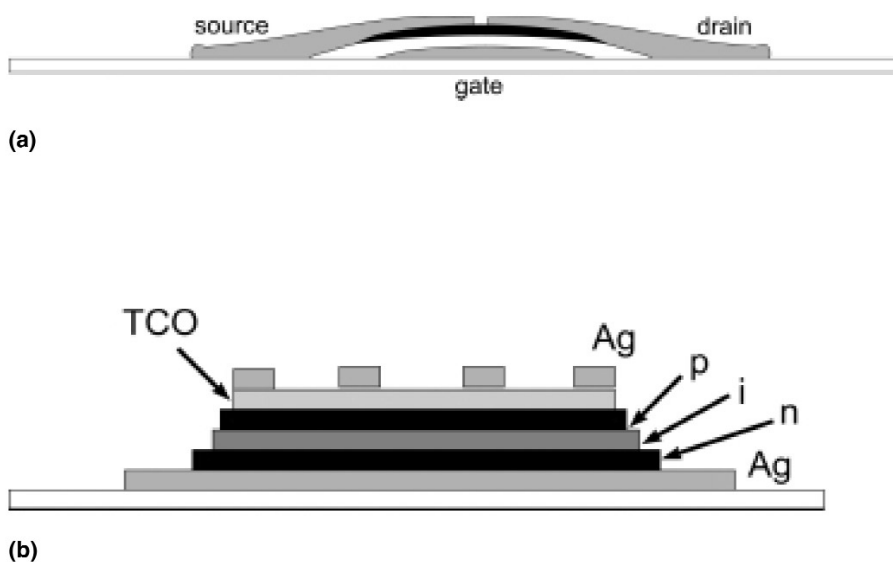


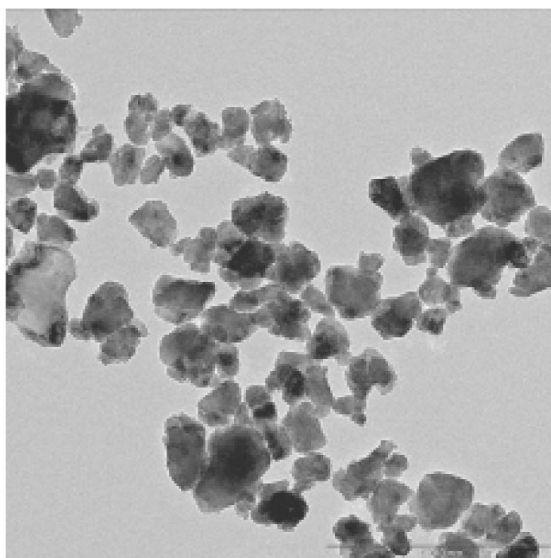
Fig. 1 Schematic diagrams of sample thick-film silicon devices, using nanoparticulate silicon inks: (a) Bottom-gate MIS-FET. The dark area is the printed nanoparticulate silicon, and the gray represents the printed silver contacts. (b) NIP photodiode structure showing the silver bottom contact, N-, I-, P-type silicon layers, the printed transparent semiconducting layer (TCO), and the painted front silver collecting grid.

The build sequence and fabrication methods for the diode structure are similar, with a layer of silver ink first printed onto the paper substrate to form the base contact. After drying in air, under ambient conditions, a layer of ink produced from the N-type material is stencil-printed onto an area of 1×1 cm, using a glass roller. This layer was allowed to cure for about 8 h under a lamp giving temperature of about 40°C . The intrinsic and the P-type layers were then deposited using the same procedure. A final window layer was applied using a commercial transparent conducting ink (Dupont 7162). Electrical contact to the window layer was achieved by painting a silver grid, leaving 9 open squares of approximately 1 mm^2 area. The average thickness of each printed layer was estimated to be approximately 100 nm. Because these layers are extremely thick, leading to essentially opaque material, light absorption in the inactive regions is expected to be high, and any photoresponse should be only a small effect.

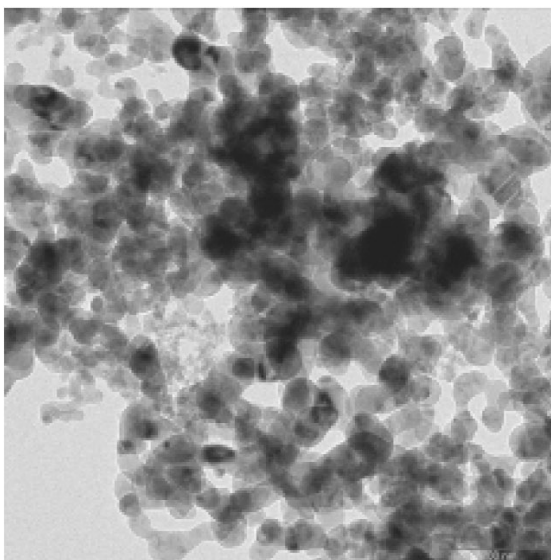
RESULTS AND DISCUSSION

Figure 2 shows TEM images of the powder milled from N-type wafers and the intrinsic powder produced by silane pyrolysis. Generally, all the milled particles have irregular shapes, with a tendency to being prolate with a definite major axis, whereas the particles produced by gas-phase synthesis are clearly uniformly round. The aspect ratio for all milled particles is approximately 3:2, but it remains unclear whether the major axis has a definite crystallographic orientation. Particles milled for longer have smaller sizes, with an average length around 200 nm after 1 h milling. There is a wide distribution of particle sizes, with particles up to a micron in length and a minimum approximately 100 nm for both the N- and P-type material. This can be attributed to the minimum, which can be achieved for single-crystalline silicon using this milling technique.

The powder milled from metallurgical-grade silicon is qualitatively different to that milled from single-crystalline material, in that the particles are generally more smooth, and the minimum size reached is considerable smaller at around 20 nm. However, the overall shape of the particles is similar, being prolate with an approximate aspect ratio of 3:2. The intrinsic particles, produced by silane de-



(a)

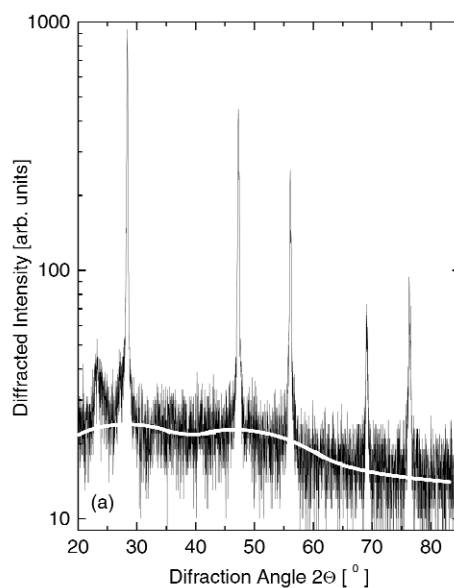


(b)

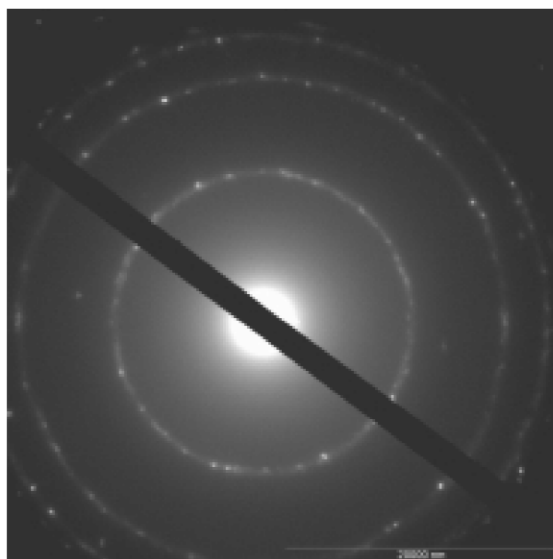
Fig. 2 TEM images of nanoparticulate silicon produced by different methods: (a) N-type single-crystal wafer milled for 60 min; (b) intrinsic nanoparticles produced by laser pyrolysis of silane.

composition, in contrast, are generally spherical, with smooth surfaces and diameters in the range 30 to 60 nm, corresponding to the manufacturer's specifications.

Figure 3a shows the X-ray diffraction pattern for nanopowder produced by milling a P-type wafer for 40 min. In all samples studied, 5 crystalline peaks, corresponding to the (111), (220), (311), (400), and (331) lattice planes, were observed. The full width at half-maximum (fwhm) of the (111) peak is



(a)



(b)

Fig. 3 (a) X-ray diffraction pattern for P-type silicon milled for 40 min. The white line shows the underlying background, which has little contribution from any amorphous phase. (b) Electron diffraction pattern for N-type silicon milled for 60 min.

slightly broadened, at 0.2° , compared to the instrumental width of 0.15° . The peak width increases to 0.26° for the intrinsic powder, indicating a smaller particle size. However, compared to the instrumental width, neither broadening is significant enough to obtain a reasonable estimate of the particle size

from the Scherer line broadening. More importantly, as can be seen in the figure, which has a logarithmic scale, there is very little amorphous diffraction contributing to the underlying broad peaks indicated in the background. No other diffraction peaks, corresponding to oxide phases, were observed.

Figure 3b shows the electron diffraction pattern for the N-type powder, produced by milling for 60 min. The patterns for all the powders are similar and show superposed rotated single-crystalline diffraction patterns, overlaying weak continuous rings. The rings have a similar width to the size of the spots, suggesting that there is little or no amorphous fraction in any of the samples. For the larger, milled, particles, it is likely that only a few individual particles are illuminated, so the presence of a large number of superposed diffraction patterns, and of the rings, suggests that these particles may be polycrystalline. This is the case even for single-crystalline starting material. For the smaller-grained intrinsic powder, it is not possible to draw any conclusion because of the large number of particles illuminated by the electron beam.

SEM micrographs of the printed layers (Fig. 4) show clustering of the individual particles, which in turn cluster to form a self-similar structure that has a continuous semiconducting backbone. All the layers exhibit the same clustering geometry, except for a scaling to the size of the particles, so that the same features are seen in the micrographs for the intrinsic particles (Fig. 4a) and the larger-milled P-type particles (Fig. 4b). Although the two images appear superficially the same, the magnification of Fig 4a is twice that of Fig 4b.

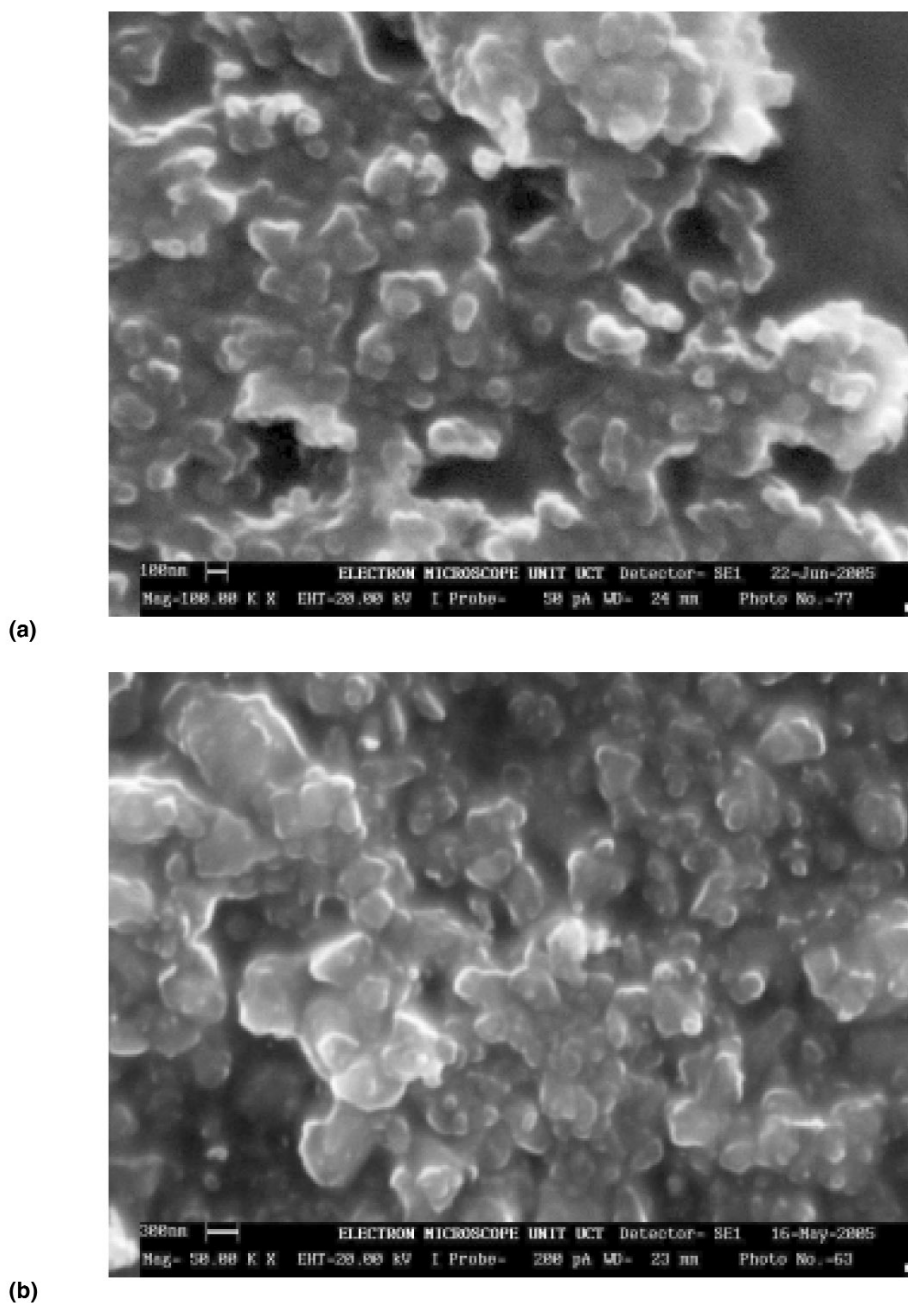


Fig. 4 Secondary electron SEM images of printed nanoparticulate silicon layers on paper substrates: (a) commercially obtained nominally intrinsic powder produced by laser pyrolysis of silane; (b) P-type silicon milled for 60 min.

In the first few hours after exposure to air, the total hydrogen and oxygen concentrations in the intrinsic nanocrystalline powder, determined using ion beam analysis methods, were 1 and 2 atom %, respectively. After one week, in air these values stabilized to 1.2 atom % hydrogen and 5 atom % oxygen (see Fig. 5). The oxygen concentration for the milled metallurgical-grade powder was slightly higher at 8 atom %, but the hydrogen content was the same at 1 atom %. Based on the size of the par-

ticles, the oxygen concentration in the intrinsic material corresponds to approximately 1 monolayer of oxide, suggesting that the surface is stabilized by oxygen termination. The slightly higher oxygen concentration in the metallurgical-grade silicon can be attributed to bulk oxygen impurities (not specified by the manufacturer), or due to the higher specific surface area of the irregularly shaped particles.

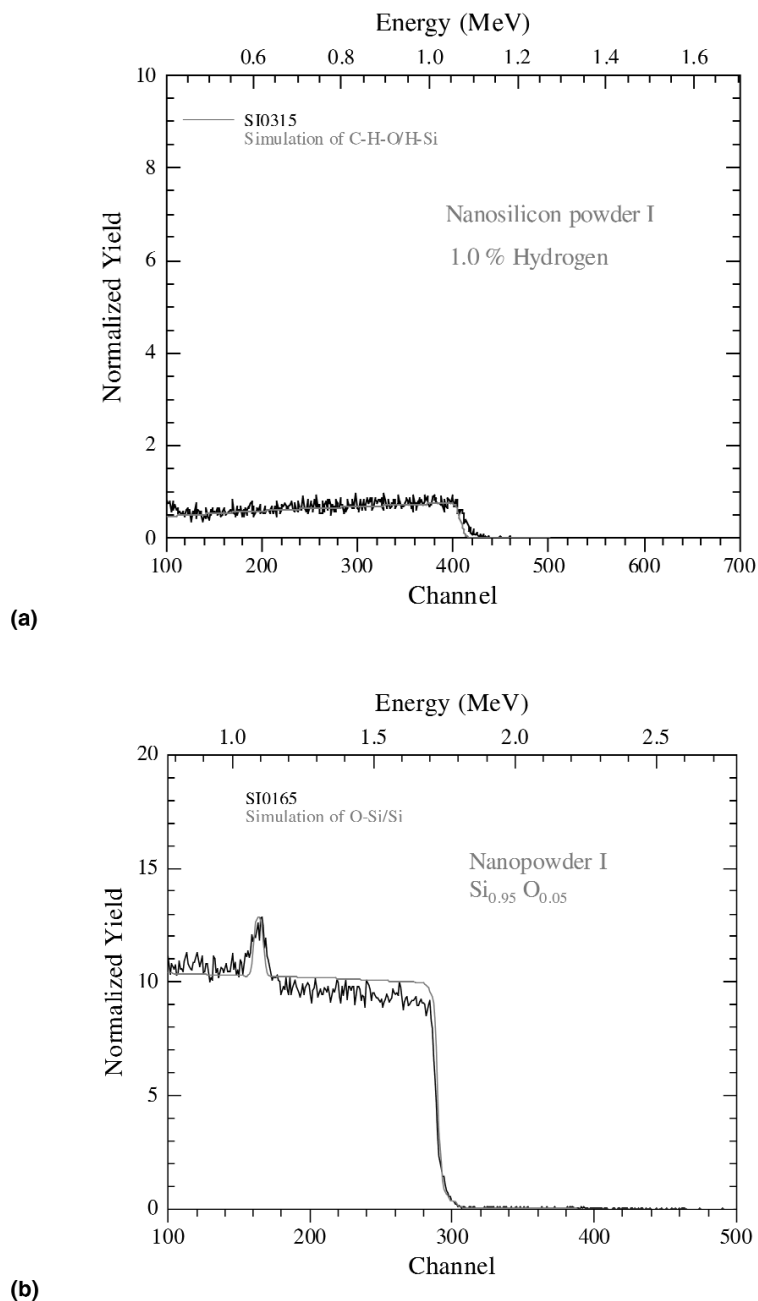


Fig. 5 (a) Elastic recoil spectrum for hydrogen in intrinsic silicon nanopowder. The solid line is a model assuming 1 atom % hydrogen concentration. (b) Rutherford back-scattering spectrum for helium ions at the 3.05 MeV oxygen resonance from intrinsic silicon nanopowder. The solid line is a model assuming a uniform 5 atom % oxygen concentration.

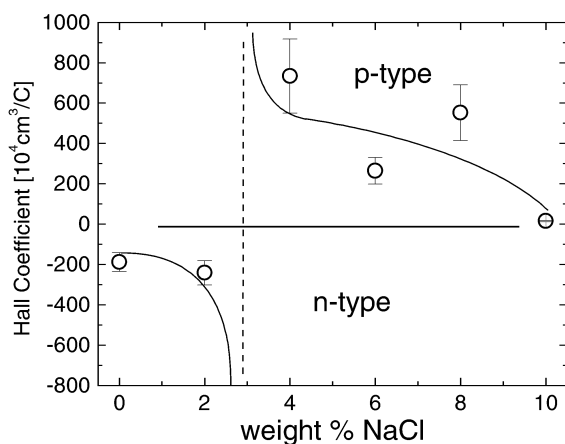
Table 1 shows the Hall characteristics of various layers produced from the different nanoparticles. Both the nominally intrinsic and metallurgical grade powders proved to be N-type, as expected. For the milled wafers, the doping type is maintained, although the resistivities are increased drastically, by four to five orders of magnitude. Not only are the resistivities of all the layers similar, but this increase is greater for the low-resistivity N-type material, suggesting that size and packing effects dominate the charge transport. Carrier mobilities are comparable to the original material, but the free carrier concentration is dramatically reduced, resulting in the increase in resistivity.

Table 1 Hall effect data for the four types of nanopowder with different volume fractions of the same binder: Because of inaccuracies in thickness determination and low currents, the data are only accurate to two significant figures. The charge of the majority carriers is given by the sign of the mobility.

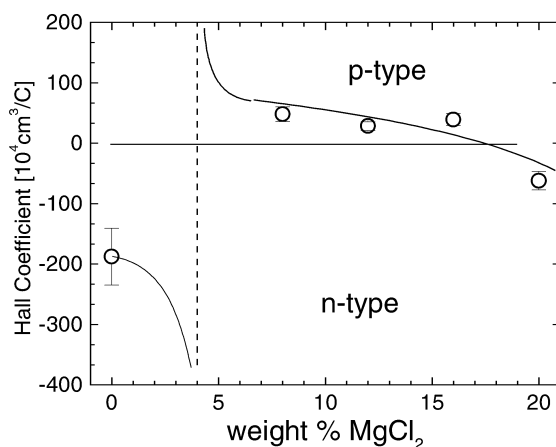
| Nanopowder | Particle vol. fraction | Resistivity M Ω cm | Hall mobility cm ² V ⁻¹ s ⁻¹ | Carrier conc. $\times 10^{12}$ cm ⁻³ |
|---------------|------------------------|---------------------------|---------------------------------------------------------------|-------------------------------------------------|
| Intrinsic | 92 % | 0.67 | -2.8 | 3.3 |
| N | 88 % | 0.26 | -1.6 | 15 |
| | 90 % | 0.29 | -1.9 | 11 |
| | 92 % | 0.32 | -1.2 | 17 |
| P | 88 % | 13 | +0.12 | 0.86 |
| | 90 % | 15.5 | +0.15 | 0.28 |
| | 92 % | 16.2 | +0.45 | 0.41 |
| Metallurgical | 91 % | 2.22 | -0.65 | 4.3 |

The reduction of carrier concentration, without reduction of mobility compared to the bulk material, suggests the introduction of deep levels in the bandgap, but no increase in the concentration of shallow levels or tail states leading to increased scattering. The high mobility also indicates good electrical conduction between the particles, confirming that the clusters form an interconnecting network, which does not inhibit charge transport. The nature of the deep traps is at present unclear, although their presence in the particles produced by gas-phase synthesis suggests that they are size-related, rather than due to mechanically induced defects. A potential defect is an infrared (IR) band at 1.6 eV, which has been observed for Si clusters in a silica matrix [8] and in mechanically milled particles [23]. The intensity of this luminescence band has been shown to increase with decreasing size, and to be inversely correlated with the conductivity [8], suggesting that this is a surface-related state. For it to be an equally efficient trap of electrons and holes, however, it would probably be an excitonic level, which still has to be confirmed. In mechanically milled particles, there is a further IR band at 0.8 eV, which has been attributed to mechanically induced defects [23]. As this is near the mid-gap position, it also cannot be excluded as contributing to the localization of charge carriers.

Figure 6 shows the behavior of the Hall coefficient, which is inversely proportional to the net carrier concentration, as a function of the amount of NaCl (Fig. 6a) or MgCl₂ (Fig. 6b) added to the mixture. At 2 % by weight NaCl, the printed layer remains N-type, but has a slightly lower carrier concentration and more negative Hall coefficient than the undoped material. Between 2 and 4 % of NaCl added, the material has changed from an N- to a P-type semiconductor. For 4 % and more NaCl added, the Hall coefficient is positive and decreases with increasing concentration. At 10 %, the Hall coefficient is very low, but remains positive. The detailed mechanisms of the doping process caused by the addition of an ionic salt are still being investigated. At present, there are two possible mechanisms. The simplest scenario is absorption or adsorption of an ion, by which a particle is then neutralized. A positively charged cation will then accept an electron from the particle, resulting in overall P-type doping. Elemental mapping, using a 120-keV STEM shows clearly that chlorine is adsorbed onto the nanoparticles, and not in the surrounding matrix. Figure 7 shows the elemental map for chlorine and the cor-



(a)



(b)

Fig. 6 Hall coefficient of nanoparticulate silicon inks doped with ionic salts (a) NaCl and (b) MgCl₂.

responding micrograph for a powder doped with 10 % NaCl. The position of the chlorine clearly corresponds to the position of the particles. Overall, this suggests another mechanism in which the anion is adsorbed, but maintains its charge state. For charge to be conserved, the particle has to change its overall charge by the opposite of that of the ion, which can occur by neutralization of a positively charged species, such as a cation, or by the ionization of a neutral species in solution.

A similar behavior is seen for doping with magnesium chloride (Fig. 6b). For 4 % doping, it was not possible to observe a Hall voltage, indicating that the carrier concentration is zero and the Hall coefficient is undefined. This suggests that the initial doping occurs by trapping or elimination of conduction electrons from the N-type particles. For additions of MgCl₂ between 4 and 16 wt %, the Hall coefficient is positive, but decreases with increasing concentration, indicating P-type conductivity. For 20 % MgCl₂, the conductivity becomes N-type again. In this case, however, it appears that the Hall coefficient passes smoothly through zero, which could be interpreted as a change in net doping type caused by competition between two effects. This could either be coadsorption of anion or cation species, or adsorption of one type of ion in two different charge states.

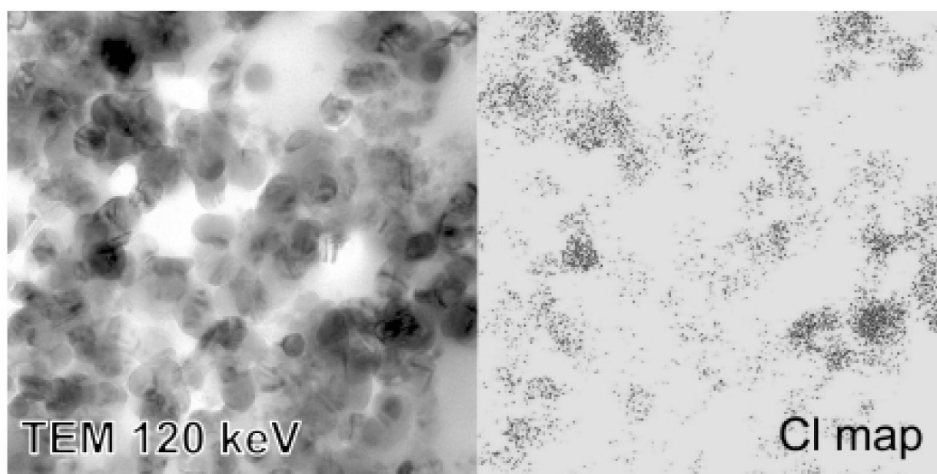
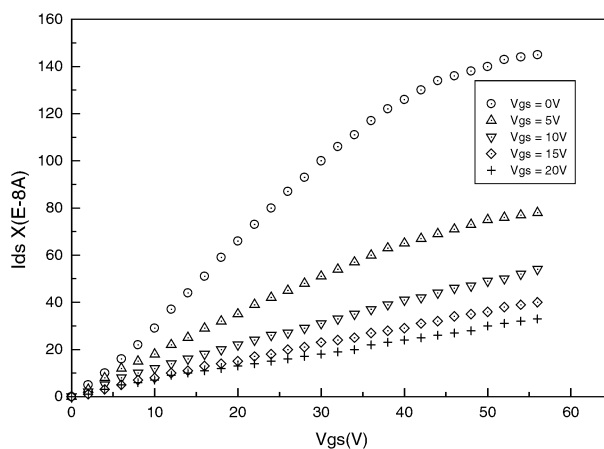
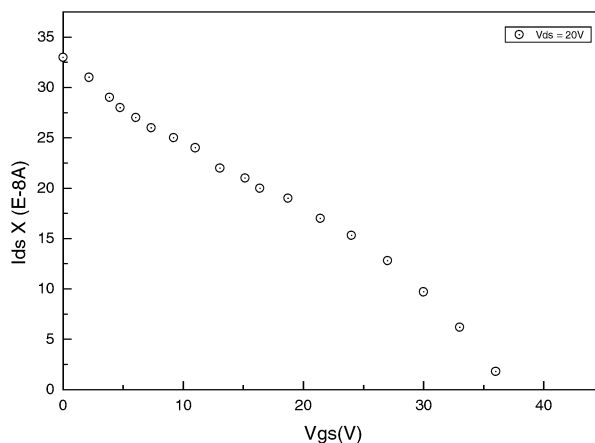


Fig. 7 TEM image (a) and corresponding elemental map of chlorine (b) for silicon nanopowder doped with 10 % NaCl by weight.

Figure 8 shows the source-drain and transfer characteristics of a typical transistor produced using the intrinsic nanoparticulate silicon with a CAB binder and gate insulator. Similar characteristics have been obtained with acrylic-based inks, except that the saturation current is considerably lower than the $1.2 \mu\text{A}$ for the device shown here. The gate capacitance for the transistor shown in Fig. 8 was determined to be 8 nF, leading to an estimate of the field effect mobility, at a drain-source voltage of 20 V, of $0.011 \text{ cm}^2 \text{ V}^{-1} \text{ s}^{-1}$. This value compares favorably with both printed organic transistors [27] and amorphous silicon transistors deposited at low temperature [28].



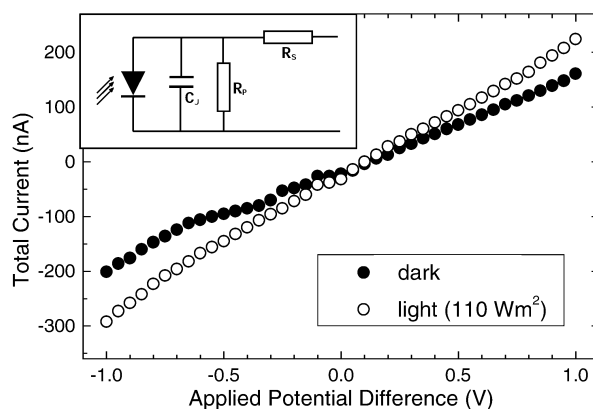
(a)



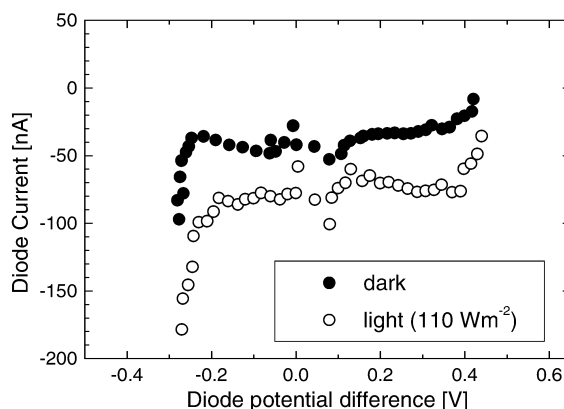
(b)

Fig. 8 Source-drain characteristics (a) and transfer characteristics (b) of a MIS-FET produced using intrinsic nanoparticulate silicon, with CAB as a binder and gate insulator material.

At first sight, the NIP diode structure appears to function simply as a resistor, albeit with some degree of photoconductivity (Fig. 9). The reason for this is the presence of parasitic series and shunt (parallel) resistances in the equivalent circuit shown in the inset. The series resistance arises from both the resistivity of the semiconductor and any contact resistances. Its effect is to reduce the effective potential difference across the diode junction, and in the ideal case should be less than a few $k\Omega$. In contrast, the shunt resistance represents a leakage current bypassing the diode junction, either through the substrate or a short circuit through the layers, resulting in a lower true current through the diode. In an ideal device, the shunt resistance should, therefore, be effectively infinite compared to all other components in the circuit. Unfortunately, for this particular device, both parasitic resistances are of the order of megaohms, leading to a flattening of the measured characteristic curve. After correction for the par-



(a)



(b)

Fig. 9 Diode characteristics of the NIP structure shown in Fig. 1b: (a) uncorrected curve as measured; (b) after correction for the shunt and series resistances in the equivalent circuit shown in the inset.

asitic resistances, the device shows a reasonable diode characteristic, with a photocurrent of approximately 40 nA, and an open circuit voltage of 0.44 V, for illumination of 110 W m^{-2} . Both of the parasitic resistances decrease on illumination, from 3.6 to 1.35 M Ω for the shunt and from 3.5 to 2.5 M Ω for the series resistance. This behavior indicates the presence of photogenerated carriers, and so suggests that the origin of both effects is in the silicon layers and not in the contact or substrate materials. The magnitude of both the observed photocurrent and the observed photoconductivity, however, are significant enough, even in this primitively fabricated device, to demonstrate the potential of the nanoparticulate silicon in both sensor and photovoltaic applications.

CONCLUSIONS

We have demonstrated the inclusion of nanoparticulate silicon as the active layer, in electronic materials, which can be printed using simple techniques on low-temperature substrates such as paper.

Particular emphasis has been placed on the structure, morphology, and composition of the nanoparticles. In general, the particles are crystalline, with a low, stable concentration of oxygen and hydrogen. Milled particles are generally irregular in shape with a definite major axis. This morphology is independent of whether the starting material is single or polycrystalline.

There are indications, from microscopy, that in the printed composite materials, the nanoparticles cluster to form a self-similar structure, leading to an interconnected backbone of semiconducting material. Electrical conductivity through this network has the characteristics of the bulk precursor material, except for a significant reduction in the carrier density. The majority carrier type and mobility are essentially unchanged compared to the bulk material.

Demonstration devices, in the form of FETs and photodiodes, based on printable silicon thick-film technology, have been presented. Although not yet of commercial quality, the material characteristics implied from the device characteristics clearly show the potential and applicability of the technique. In particular, field effect mobilities and saturation currents, comparable to those found in existing technologies, such as organic and silicon thin-film electronics, have been obtained. A clear photoelectric response, with potential applications in photovoltaic conversion and optical sensors, has also been shown.

ACKNOWLEDGMENTS

The results discussed above are a representative selection of over two years work produced by our research group and collaborators. The following students and colleagues have been instrumental in both producing the samples and obtaining the experimental data: Ayodele Odo, Girma Goro, Olusegun Adegbite, Fhatuwani Nematili, Tshilidzi Thovhogi, Tshepho Ntsoane, Prof. Craig Comrie, and Dr. Mohammed Jaffer.

REFERENCES

1. P. J. Holmes, R. G. Loasby. *Handbook of Thick-Film Technology*, Electrochemical Publishing, Ayr, Scotland (1974).
2. G. Hodes, D. Cahen, J. Manassen, M. David. *J. Electrochem. Soc.: Sol. State Sci. Technol.* **127**, 2252 (1980).
3. M. Boehm. Particulate Semiconductor Devices and Methods, U.S. Patent 497219, filed 6 January 1987, granted 7 August 1990.
4. G. Ambrosone, U. Coscia, R. Murri, N. Pinto, M. Ficcadenti, L. Morresi. *Sol. Energy Mater. Sol. Cells* **87**, 375 (2005).
5. A. Gordijn, J. K. Rath, R. E. I. Schropp. *J. Non-Cryst. Solids* **338–340**, 110 (2004).
6. H. Fujiwara, M. Kondo, A. Matsuda. *J. Non-Cryst. Solids* **338–340**, 97 (2004).
7. F. Yun, B. J. Hinds, S. Hatatani, S. Oda, Q. X. Zhao, M. Willander. *Thin Solid Films* **375**, 137 (2000).
8. I. Balberg, E. Savir, J. Jedrzejewski. *J. Non-Cryst. Solids* **338–340**, 102 (2004).
9. G. A. Kachurin, I. E. Tyschenko, K. S. Zhuravlev, N. A. Pazdnikov, V. A. Volodin, A. K. Gutakovsky, A. F. Leier, W. Skorupa, R. A. Yankov. *Nucl. Instrum. Methods Phys. Res., Sect. B* **122**, 571 (1997).
10. S. Thompson, C. R. Perrey, C. B. Carter, T. J. Belich, J. Kakalios, U. Kortshagen. *J. Appl. Phys.* **97**, 034310 (2005).
11. A. S. Gudovski, J. P. Kleider, V. P. Afanasejev, A. Z. Kazak-Kazakevich, A. P. Sazanov. *J. Non-Cryst. Solids* **338–340**, 135 (2004).
12. M. Ando, H. Miyamoto, H. Naito, Y. Kanemitsu. *J. Non-Cryst. Solids* **299–302**, 1084 (2002).
13. K. Tonokura, T. Murasaki, M. Koshi. *J. Phys. Chem. B* **106**, 555 (2002).
14. V. G. Kravets, C. Meier, D. Konjhodzic, A. Lorke, H. Wiggers. *J. Appl. Phys.* **97**, 084306 (2005).

15. M. Ehbrecht, F. Huisken. *Phys. Rev. B* **59**, 2975 (1999).
16. W. S. Cheong, N. M. Hwang, D. K. Yoon. *J. Cryst. Growth* **204**, 52 (1999).
17. H. Hofmeister, P. Kodderitzsch, J. Dutta. *J. Non-Cryst. Solids* **234**, 182 (1998).
18. T. Seto, T. Orii, M. Hirasawa, N. Aya. *Thin Solid Films* **437**, 230 (2003).
19. X. M. Lu, T. Hanrath, K. P. Johnston, B. A. Korgel. *Nano Lett.* **3**, 93 (2003).
20. Q. Liu, S. M. Kauzlarich. *Mater. Sci. Eng. B* **96**, 72 (2002).
21. J. P. Wilcoxon, G. A. Samara, P. N. Provencio. *Phys. Rev. B* **60**, 2704 (1999).
22. V. Švrček, J.-L. Rehspringer, E. Gaffet, A. Slaoui, J.-C. Muller. *J. Cryst. Growth* **275**, 589 (2005).
23. C. Díaz-Guerra, A. Montone, J. Piqueras, F. Cardellini. *Semicond. Sci. Technol.* **17**, 77 (2002).
24. C. Araujo-Andrade, F. J. Espinoza-Beltrán, S. Jiménez-Sandoval, G. González-Hernández. *Scr. Mater.* **49**, 773 (2003).
25. D. T. Britton, M. Härting, D. Knoesen, Z. Sigcau, F. P. Nematlili, T. P. Ntsoane, P. Sperr, W. Egger, M. Nippus. *Thin Solid Films* **501**, 79 (2006).
26. L. R. Doolittle. *Nucl. Instrum. Methods Phys. Res., Sect. B* **15**, 227 (1986).
27. T. G. Bäcklund, H. G. O. Sandberg, R. Österbacka, H. Stubb, T. Mäkela, S. Jussila. *Synth. Met.* **148**, 87 (2005).
28. J. P. Conde, P. Alpuim, V. Chu. *Thin Solid Films* **430**, 240 (2003).